Synthesis, Crystal Structure, and Physical Properties of BaAg$_2$Cu[VO$_4$]$_2$: A New Member of the $S = {}^1\!/_2$ Triangular Lattice

Ngozi E. Amuneke,[†,‡] Dana E. Gheorghe,[†,‡] Bernd Lorenz,[‡,§] and Angela Möller*[,†,‡]

[†]Department of Chemistry, University of Houston, 136 Fleming Building, Houston, Texas 77204-5003, United States
[‡]Texas Center for Superconductivity, University of Houston, 2002 Houston Science Centre, Houston, Texas 77204-5002, United States
[§]Department of Physics, University of Houston, 617 Science & Research Building 1, Houston, Texas 77204-5005, United States

S *Supporting Information*

ABSTRACT: By application of flux growth methods in combination with redox reactions, single crystals of BaAg$_2$Cu[VO$_4$]$_2$ can be synthesized. A new structure type (triclinic, $P\bar{1}$, $Z = 2$, $a = 5.448(2)$ Å, $b = 5.632(3)$ Å, $c = 14.393(6)$ Å, $\alpha = 94.038(9)°$, $\beta = 90.347(6)°$, and $\gamma = 118.195(5)°$) has been found and will be described here. Structure-properties relationships have been investigated by spectroscopic methods (IR, UV−vis−NIR, ESR) and the electronic structure will be discussed within the angular-overlap model (AOM) for Cu^{2+}. Furthermore, we present the magnetization and specific heat data for BaAg$_2$Cu[VO$_4$]$_2$ representing a Heisenberg spin system with exclusive super-super exchange (SSE) on a frustrated magnetic triangular lattice. Considerable antiferromagnetic (AFM) low-dimensional interaction is evident, and ferromagnetic-like long-range order sets in at ≈0.7 K.
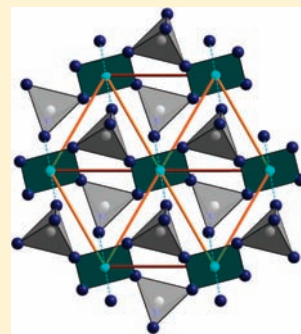
1. INTRODUCTION

Low-dimensional spin systems have attracted considerable interest because of their rich physics with respect to the novelty of ground states and excitations such systems may exhibit.[1] In recent years it has been established that not only superexchange (SE) pathways as described by Goodenough can be the dominating magnetic nearest neighbor interaction,[2] but also super-super exchange (SSE) via phosphates and vanadates is likely to play a major role in the evaluation of low-dimensional magnetic properties.[3] Lately, conclusions drawn from experimental work, mainly magnetization and specific heat measurements, have received extensive theoretical support by band structure calculations based on density functional theory (DFT), mapping the relevant local density approximation (LDA) bands onto a tight binding (TB) model and subsequently onto a Hubbard and Heisenberg model.[4] Examples for one-dimensional (1D) spin systems following the behavior of a Heisenberg antiferromagnet ($H = J_{intra}\sum_i S_i \cdot S_{i+1}$) in a wide temperature range are, for example, AgCuVO$_4$ (SE, $J_{intra} \approx 330$ K)[5] and Ba$_2$Cu[PO$_4$]$_2$ (SSE, $J_{intra} = 151(6)$ K).[6] At low temperatures interchain correlations often lead to long-range magnetic order, with $T_N = 2.5$ K in the first case, but were not observed for the latter compound down to temperatures as low as 0.45 K. Many phosphates have been studied yielding a consistent picture of the exchange parameter, J_{intra}, relating to a SSE pathway, whereas a few cuprates consisting of solely vanadate bridging features have been studied in detail so far. One recent report describes ACuV$_2$O$_7$ (A = Sr, Ba) as a rare example for a ferromagnetic 1D zigzag spin system.[7]

Motivated by structure-properties relationships outlined above, we focused our work on layered vanadates exhibiting solely SSE interactions. In this respect, we will report on a new member, BaAg$_2$Cu[VO$_4$]$_2$, of the BaA$_2$M[VO$_4$]$_2$ family of compounds with M = Cu, Mn; A = Ag, Na. The crystal structure of BaAg$_2$Cu[VO$_4$]$_2$ is only fairly related to BaNa$_2$Cu[VO$_4$]$_2$ and significantly different from BaAg$_2$Mn[VO$_4$]$_2$.[8,9] Although many examples of isotypic structures for Na and Ag compounds have been reported, this is not the case here. Furthermore, the distortions occurring in these structures are related to differences in the coordination of Ag and Na, as well as in the electronic structures of the $S = {}^1\!/_2$ (Cu^{2+}) and $S = {}^5\!/_2$ (Mn^{2+}) magnetic ions. In principle, the magnetic ions form a two-dimensional (2D) triangular lattice with $d(M-M) \approx 5.5$ Å exclusively interconnected via vanadate ions as a common feature, matching the requirements for the above-mentioned guidelines for AFM SSE pathways of $\angle(M-O\cdots O) \approx 113°$ and $145°$. Notably, the O$\cdots$O distance is in general larger by ≈0.4 Å in vanadates compared with phosphates, which will reduce the effective overlap and thereby lead to smaller J values. On the other hand, a partial contribution of the vanadium d-orbitals dissimilar to the phosphates might play a subtle role leading to remarkable differences in exchange interactions. Furthermore, frustrated spin arrangements can cause a reduction of the overall effective exchange parameter, which might provide one way to access regions in the phase diagram close to quantum criticality (quantum spin liquids), for example, BaCdVO[PO$_4$]$_2$ or Li$_2$ZrCuO$_4$.[10,11]

In this work we will outline the synthesis and the new crystal structure of BaAg$_2$Cu[VO$_4$]$_2$. Spectroscopic details provide

valuable insights into the electronic structure of the $[CuO_{4+2}]$ entities and will be described within a ligand field approach (angular-overlap model, AOM).[12] Electron spin resonance (ESR) and temperature dependent susceptibility data have been derived from this model and will be compared with experimental data. Low-temperature magnetic and specific heat data are presented to explore the features of a $S = {}^1/_2$ triangular lattice.

2. EXPERIMENTAL SECTION

Synthesis. Amber single crystals of $BaAg_2Cu[VO_4]_2$ were synthesized from cesium hydroxide fluxes in Ag-containers at 550 °C using 306.7 mg of CsOH (99.9% metals basis; Alfa Aesar), 41.1 mg of CuO (Coleman Instruments Corp.), 95.9 mg of V_2O_5 (Alfa Aesar), and 160.5 mg of $Ba(OH)_2 \cdot 8H_2O$ (minimum 98.0%; Sigma-Aldrich Chemie) as starting materials in a 4:1:1:1 molar ratio. Unlike in sodium or potassium hydroxide melts significant oxidation of silver occurs in cesium hydroxide as a flux and thereby enabling crystal growth of novel silver vanadates in ambient atmosphere.

The reaction was kept at 420 °C for 3 weeks, increased to 550 °C for 3 days, and then slowly cooled within 2.5 days to room temperature. Apart from the solidified flux components (gray powder), few dark red crystals of $BaCu_2[VO_4]_2$ were identified by X-ray diffraction experiments revealing a perfect match with the reported crystal structure data.[13] The main product of harvested single crystals consisted of a dark orange-yellow color and proved to be the new title compound. Energy Dispersive X-ray (EDX) analysis of several crystals confirmed the composition ratio Ba/Ag/Cu/V of 1:2:1:2 with averaged observed atomic-% of 17.0(2); 37(1); 14.1(7); 31.5(5), respectively. The measurement was carried out using a JSM 6330F (JEOL) with a 15 kV accelerated voltage and a 12 μA beam current alongside with an Oxford analyzer (ISIS). $BaSO_4$, Ag metal, V metal, and CuO were used as standards.

Powder samples of $BaAg_2Cu[VO_4]_2$ were prepared from Ag_2O (Pfaltz & Bauer, Inc.), V_2O_5, CuO, and either $Ba(OH)_2 \cdot 8H_2O$, or $BaCO_3$ (Matheson, Coleman, & Bell), respectively, in alumina boats at 550 °C for 3 days in air. $BaAg_2Cu[VO_4]_2$ could be obtained as phase pure polycrystalline samples according to X-ray diffraction data (X'Pert Pro PANanalytical; Anton Paar) using the two sources of barium compounds as starting materials, respectively. Lattice constants ($a = 5.4419(2)$ Å; $b = 5.6219(3)$ Å; $c = 14.3657(6)$ Å; $\alpha = 94.227(4)°$; $\beta = 90.472(4)°$; $\gamma = 118.052(4)°$; $V = 386.36(3)$ Å^3, $R_{Bragg} = 2.79$, $R_f = 2.28$, $\chi^2 = 1.16$) have been refined by a LeBail fit using the program Fullprof.[14] Furthermore, infrared data revealed no sign of any of the starting materials indicating completion of the reaction. The new compound $BaAg_2Mg[VO_4]_2$, isotypic with $BaAg_2Mn[VO_4]_2$, has been prepared from reacting $BaCO_3$, Ag_2O, V_2O_5, and $MgCO_3$ [$(MgCO_3)_4 \cdot Mg(OH)_2 \cdot 4H_2O$; Reagent grade] in a 1:1:1:1 ratio at 550 °C as a reference for the lattice contribution to the specific heat. $BaAg_2Mg[VO_4]_2$ crystallizes in the space group, $P\bar{3}$, with lattice constants $a = 5.5249(2)$ Å, $c = 7.2003(1)$ Å, $V = 190.344(7)$Å^3, $R_{Bragg} = 1.48$, $R_f = 1.3$, $\chi^2 = 1.55$, LeBail fit.

Crystal Structure Determination. A block-shaped crystal with edges of approximately $0.05 \times 0.1 \times 0.15$ mm^3 was selected under Paratone-N oil (Hampton Research) and mounted on a glass fiber. A single crystal data set of 2363 reflections was collected on an APEX II CCD Detector Bruker AXS instrument at room temperature. The unit cell parameters for the space group $P\bar{1}$ were determined from 1345 reflections using the program SAINT (V-7.60A, Bruker). Absorption correction was applied using MULTISCAN[15] implemented in WinGX[16] yielding the experimental transmission coefficients $T_{min} = 0.1091$ and $T_{max} = 0.1831$. Data reduction was applied to merge multiple determined reflections resulting in an overall unique data set of 1690 independent reflections ($R_{int.} = 0.019$) with a 95% completeness for

Table 1. Crystal Data and Details of the Structure Determination for $BaAg_2Cu[VO_4]_2$

formula	$BaAg_2CuV_2O_8$ (M_r = 646.50 g/mol)
crystal system	triclinic
space group	$P\bar{1}$ (No. 2); $Z = 2$
lattice constants	$a = 5.448$ (2) Å
	$b = 5.632$ (3) Å
	$c = 14.393$ (6) Å
	$\alpha = 94.038$ (9)°
	$\beta = 90.347$ (6)°
	$\gamma = 118.195$ (5)°
V	387.9 (3) Å^3
D_{calcd}	5.536 g cm^{-3}
μ(Mo K$_\alpha$)	14.96 mm^{-1} ($\lambda = 0.71073$ Å)
$F(000)$	578
temperature	296(2) K
range	$\Theta_{min} = 2.8°$; $\Theta_{max} = 28.3°$
data set	$-7 \leq h \leq 5$
	$-7 \leq k \leq 7$
	$-18 \leq l \leq 14$
unique data, R_{int}	1690; 0.019
parameter refined	131
R_1, $wR2$	0.040, 0.107

the measured hkl data range. The structure solution was obtained from Direct Methods[17] and the resulting atomic positions for Ba and Ag were used for the starting model. All other atom sites have been retrieved from Difference-Fourier-Synthesis methods,[17] and finally all positions and anisotropic thermal displacement factors were refined. Table 1 includes crystallographic data details of the structure refinement (for further information see Supporting Information). The final structure solution passed the cif and fcf check routine using PLATON.[18] Diamond[19] was used for the graphical illustration of the structure.

Physical Properties. $BaAg_2Cu[VO_4]_2$ has been studied by spectroscopic methods as well as by magnetic measurements using a Quantum Design MPMS SQUID magnetometer. MIR and UV–vis–NIR data were collected in reflectance mode on an Alpha-P (Bruker Optik) and Varian Cary 500 Scan, spectrometer, respectively. X-band ESR measurements were performed on a Bruker BioSpin instrument. The low-temperature heat capacity was measured above 0.5 K by a relaxation method using the ^{3}He option of the Physical Property Measurement System (PPMS, Quantum Design).

3. RESULTS AND DISCUSSION

The structures of $BaAg_2Mn[VO_4]_2$[8] and $BaNa_2Cu[VO_4]_2$[9] are similar to that of $BaAg_2Cu[VO_4]_2$, but not isotypic. Therefore, we will refer to the detailed structure description reported and focus our discussion here more on the differences and aspects of structure-property relationships.

Crystal Structure. $BaAg_2Cu[VO_4]_2$ crystallizes in the triclinic space group $P\bar{1}$; for further details see Table 1 and the Supporting Information. For the evaluation of the crystal structure solution and distances related to the respective naïve coordination number (C.N.) we performed calculations based on the Madelung part of the lattice energy (MAPLE[20]). The overall consistency of the structure solution can be expressed by the MAPLE value of a polynary ionic structure in comparison with the binary compounds. For $BaAg_2Cu[VO_4]_2$ we calculated a MAPLE value of 50904 kJ/mol in consistency with the sum of the binary compounds (50674 kJ/mol). The deviation of 0.45%

Table 2. Selected Interatomic Distances and MEFIR Values in Å, and ECoN Values for BaAg$_2$Cu[VO$_4$]$_2$[a]

Ag1–O8 2.364 (6) *1.14*	Ag2–O3 2.406 (6) *1.15*
Ag1–O2 2.384 (6) *1.09*	Ag2–O5 2.436 (6) *1.08*
Ag1–O1 2.416 (6) *1.01*	Ag2–O7 2.443 (6) *1.07*
Ag1–O6 2.463 (7) *0.90*	Ag2–O4 2.471 (6) *1.00*
	Ag2–O7 2.585 (7) *0.73*
ECoN 4.3; MEFIR: 1.02	ECoN 5.2; MEFIR: 1.04
Cu1–O1 1.973 (6) (2×) *1.05*	Cu2–O4 1.959 (6) (2×) *1.06*
Cu1–O2 1.974 (6) (2×) *1.05*	Cu2–O3 1.969 (6) (2×) *1.03*
Cu1–O8 2.436 (6) (2×) *0.09*	Cu2–O7 2.444(6) (2×) *0.08*
ECoN: 4.4 MEFIR: 0.63	ECoN: 4.3 MEFIR: 0.63
V1–O1 1.749 (6) *0.89*	V2–O4 1.755 (6) *0.88*
V1–O2 1.741 (6) *0.92*	V2–O3 1.757 (6) *0.87*
V1–O8 1.712 (6) *1.02*	V2–O7 1.713 (6) *1.02*
V1–O5 1.681 (7) *1.13*	V2–O6 1.675 (7) *1.16*
ECoN: 4.0 MEFIR: 0.38	ECoN: 4.0 MEFIR: 0.38
(V1–O)$_{av.}$ 1.72	(V2–O)$_{av.}$ 1.72
Ba–O4 2.745 (6) *1.31*	Ba–O5 2.968 (7) *0.85*
Ba–O8 2.820 (7) *1.16*	Ba–O5 3.072 (7) *0.65*
Ba–O3 2.827 (6) *1.15*	Ba–O6 3.092 (7) *0.62*
Ba–O1 2.860 (6) *1.08*	Ba–O6 3.112 (7) *0.58*
Ba–O2 2.900 (6) *0.99*	
Ba–O7 2.928 (7) *0.94*	ECoN: 9.5 MEFIR: 1.47

[a] Excluded distances larger than 3.0 Å for Ag–O and 3.4 Å for Ba–O, respectively, with ECoN contribution less 10%. Partial ECoN values given in italic.

is well within the 1% limit for a consistent structure refinement. Further insights for the description of a crystal structure can be gained from evaluating the interatomic distances, effective coordination numbers (ECoN), and mean effective ionic radii (MEFIR).[21] On the basis of these values which are incorporated in Table 2, we note that (a) the two crystallographic independent sites for Ag show indeed differences in their C.N.; (b) the axial oxygen atoms of the [CuO$_{4+2}$] units are almost insignificantly adding to ECoN, but are not entirely negligible for the ligand field splitting of Cu^{2+} (see section below).

A perspective view of the crystal structure is shown in Figure 1, representing a layered type of structure with respect to the copper/ortho-vanadate segments separated by barium ions along [001] as a prominent structural feature. The stacking sequence ···ABAB··· is related to Cu1 and Cu2 as the central feature, respectively, and reveals a canted orientation of the planar [CuO$_4$] plaquettes forming chains along [100] within each layer. The two crystallographic independent copper sites are rather similar with respect to their coordination spheres and connectivity. Selected interatomic distances and angles are included in Table 2 (see also Supporting Information) and corroborate the local structure similarities of the independent sites for copper.

For the divalent copper ions a typical 4 + 2 coordination is observed with equatorial distances to oxygen, Cu–O(1–4)^{eq}, of 1.97 Å (ECoN = 1.05) and axial distances, Cu–O(7,8)^{ax}, of 2.44 Å (ECoN = 0.08), respectively. The magnetic copper ions form a $S = {}^1/_2$ triangular lattice with (Cu–Cu) ≈ 5.5 Å. The connectivity is established exclusively through bridging [VO$_4$] units
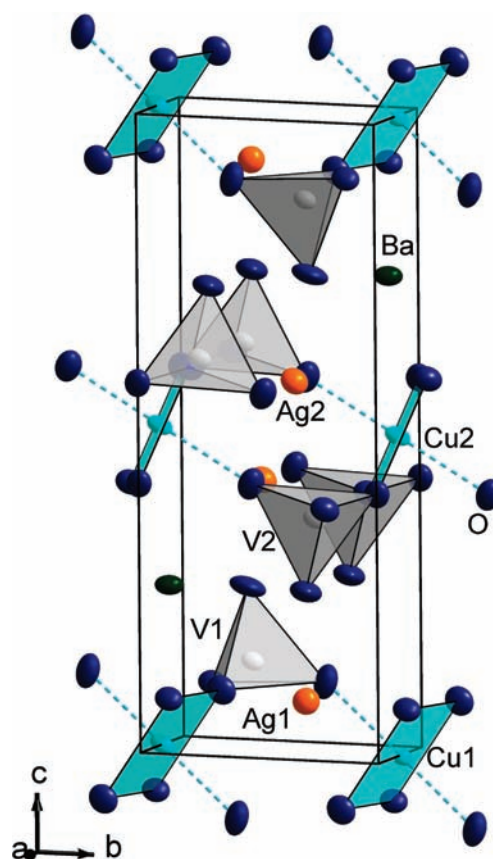

Figure 1. Perspective view of the crystal structure of BaAg$_2$Cu[VO$_4$]$_2$ with thermal ellipsoids of 75% probability. The Cu–O plaquettes are defined by the equatorial distances to oxygen (O^{eq}) whereas the axial ones (O^{ax}) are depicted as dotted lines.
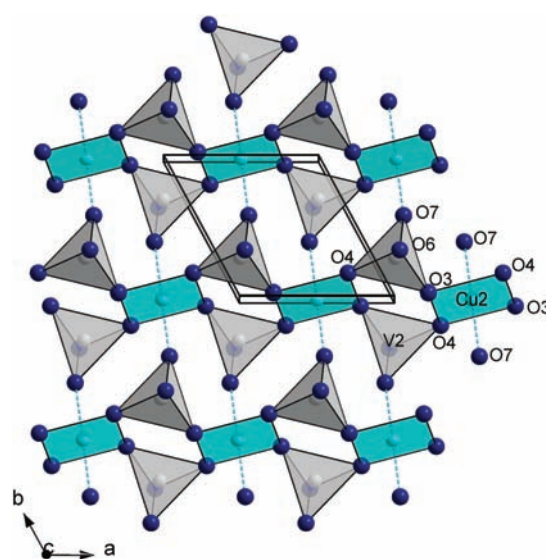

Figure 2. Layer of interconnected [CuO$_{4+2}$] and [VO$_4$] entities in BaAg$_2$Cu[VO$_4$]$_2$ depicted for the [V2O$_4$]-Cu2-[V2O$_4$] part. The same pattern is observed for the [V1O$_4$]-Cu1-[V1O$_4$] segment.

above and below the plane defined by copper. Chains of ····(O–V–O)$_2$-Cu-(O–V–O)$_2$-Cu-··· for the equatorial connectivity of the [CuO$_4^{eq}$] plaquettes result along [100] (Figure 2).

The bridging $[VO_4]$ units connect the magnetic ions asymmetrically with $\angle(Cu1-O1-O2)$, $(Cu2-O4-O3) = 113°$ and $\angle(Cu1-O2-O1)$, $(Cu2-O3-O4) = 145°$, respectively. These findings are comparable with the geometrical data relation to the SSE pathway, J_3 and J_3', in $Rb_2Cu_2[MoO_4]_3$ which are considered to be the strongest AFM interactions for that compound.[3] It should be noted that the electronic ground state of Cu^{2+} is $(x^2 - y^2)$ in $BaAg_2Cu[VO_4]_2$, see below, and therefore this pathway should be relevant for the magnetic exchange within the chain here. In contrast, the axial $Cu-O^{ax}$ direction corresponds to the magnetic interaction pathway via the fully occupied d_{z^2} orbital and is therefore often assumed to provide no significant contribution. To complete the structural description of these layers, it is worth mentioning that further linkage between the above classified chains occurs via the axial oxygen $(O7,8)^{ax}$ of the $[CuO_{4+2}]$ complex. Thereby, one $[VO_4]$ unit connects three magnetic ions altogether with one presumably dominant SSE pathway involving equatorial $Cu-O^{eq}\cdots O^{eq}-Cu$ and two exchange pathways via $Cu-O^{ax}\cdots O^{eq}-Cu$.

The two crystallographic distinguishable $[VO_4]$ tetrahedra exhibit average V–O distances of 1.72 Å corresponding to an ECoN value close to 1.0 and average angles of 109.4° within the typical range reported for ortho-vanadates. Our infrared spectroscopy data nicely confirmed the presence of the ortho-vanadate ion in $BaAg_2Cu[VO_4]_2$. Assignments based on T_d symmetry are referenced as $\nu_1 = 826$ cm^{-1}; $\nu_3 = 804$ cm^{-1}; $\nu_2 \approx \nu_4 = 366$ cm^{-1}.[22] For $BaAg_2Cu[VO_4]_2$ we observe a strong broad band centered at 730 cm^{-1} typical of the infrared-active asymmetric V–O vibrations (ν_3) and a fairly weak in intensity one corresponding to the symmetric mode (ν_1) at 872 cm^{-1}. Because of the lower symmetry of the two distorted $[VO_4]$ groups in this structure, see Table 2, a pronounced splitting of the ν_3(V–O) assigned band is anticipated and in line with the observation of broadening. One very short V–(O5,6) and three longer V–O distances are present here. The latter are associated with the connectivity of $[CuO_{4+2}]$ and $[VO_4]$ entities and nicely reveal the dependence of coordinating via $O(1-4)^{eq}$ versus almost non-coordinating oxygen via $(O7,8)^{ax}$ for Cu^{2+}. Hence, with $d(V2-O7)$ and $d(V1-O8) = 1.71$ Å the exact distance for a "free" ortho-vanadate is observed. It is conceivable that the shortest distances V–(O5,6) = 1.68 Å are associated with the top and bottom of the layer and exclusively involved in connecting to Ag and Ba. On the basis of these inherent differences in the chemical environment of the ortho-vanadate, we consider the symmetry of $[VO_4]$ unit close to C_{3v} in this case, placing the symmetry axis along the shortest V–(O5,6) distance. Thereby, the latter responds to the symmetric mode (ν_1) which is significantly shifted to higher wavenumbers compared with the "free" vanadate here. Applying the empirical relation[23] of the Raman frequency dependence (corresponding to the symmetric stretching mode, ν_1) on the interatomic distance (see also ref 24), we find that for $d(V-O) = 1.67$ Å the frequency of 868 cm^{-1} is expected. This is in excellent agreement with our observation of 872 cm^{-1}. In principle, the shift to lower wavenumbers for the triply degenerate asymmetric stretching frequency, ν_3, by almost 70 cm^{-1} can be understood as a result of an elongation of the V–O distance from 1.71 Å to 1.75 Å which is observed here. Overall, these findings reflect the difference in the connectivity of the ortho-vanadate related to the structural features particularly within a layered segment and the more ionic counterpart of separating Ba ions.
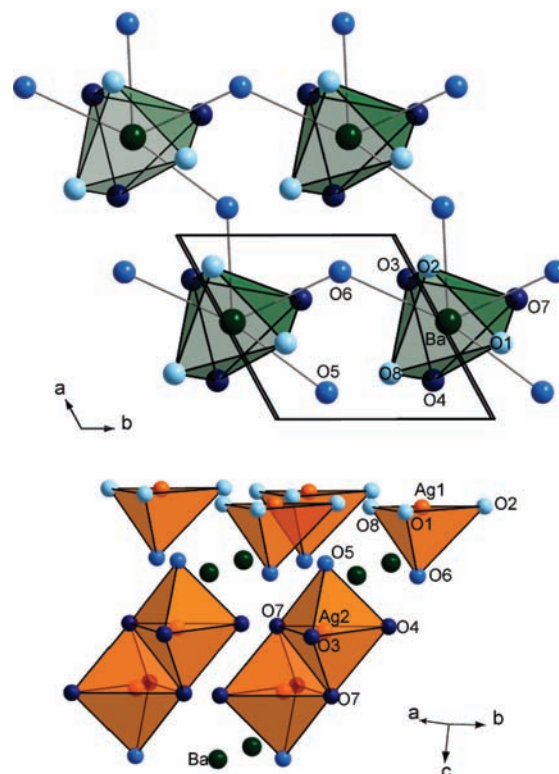

Figure 3. Top: Layer of interconnected $[BaO_{6+4}]$ entities in $BaAg_2Cu[VO_4]_2$. O1, O2, O8 (light-blue, above) and O3, O4, O7 (dark blue, below) belong to separate $[VO_4]$-Cu-$[VO_4]$ segments. The bridging oxygen atoms O5 and O6 (medium blue) belong to the top and bottom part of adjacent segments and are almost in-plane with the Ba atoms. Bottom: With reference to the color code introduced above the two distinguishable polyhedra of $[Ag1O_4]$ and $[Ag2O_5]$ are shown, as well as the edge-sharing intralayer connectivity via O7. Interlayer connectivity via O5 and O6 occurs exclusively via Ba and Ag. For simplicity V and Cu atoms have been omitted.

The coordination sphere of barium resembles a distorted elongated octahedron (O1–4,7,8) with four capping oxygen (O5,6) shared with crystallographic identical barium atoms in the a-b plane (Figure 3). The Ba–O distances, = 2.93 Å, are in good agreement with the Shannon ionic radii.[25] Note that the naïve C.N. of 10 and the polyhedron for Ba is very similar to that in $BaNa_2Cu[VO_4]_2$,[9] but different from the almost ideal cube-octahedral coordination sphere in $BaAg_2Mn[VO_4]_2$.[8]

We observe two crystallographic independent sites for silver represented by distorted isolated tetrahedral, $[Ag1O_4]$, and dimeric edge-sharing trigonal-bipyramidal $[O_3Ag2O_{2/2}Ag2O_3]$ units, respectively (Figure 3). It is interesting to note that for $BaAg_2Mn[VO_4]_2$ a distorted tetrahedral $[AgO_4]$, and for $BaNa_2Cu[VO_4]_8$ a trigonal-bipyramidal $[NaO_5]$ coordination, have been reported, placing $BaAg_2Cu[VO_4]_2$ as a missing link between the two known structure types. For this family of compounds, segments built of $[VO_4]$-Cu-$[VO_4]$ contain $[AgO_4]$ entities in each of the vanadate layers (Figure 3) resulting in a honeycomb pattern of alternating Ag and V atoms. The differences in ionic radii for these give rise to distortions within the layered segments resulting in asymmetric bridged $[CuO_{4+2}]$ entities relevant for SSE pathways. On the other hand, a slightly different orientation of the $[CuO_4]$ plaquettes in every second layer effectively alters the C.N. of Ag, in this case from four to five.
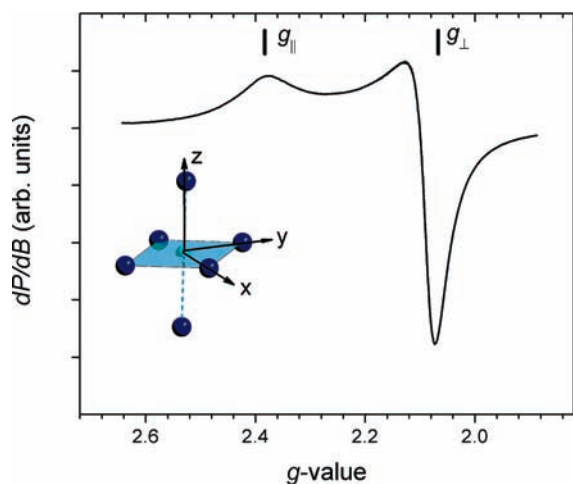
Figure 4. X-Band ESR spectrum for $BaAg_2Cu[VO_4]_2$. The calculated g-values (black, line markers) with respect to D_{4h} symmetry (see inset for referenced molecular axis) are included.
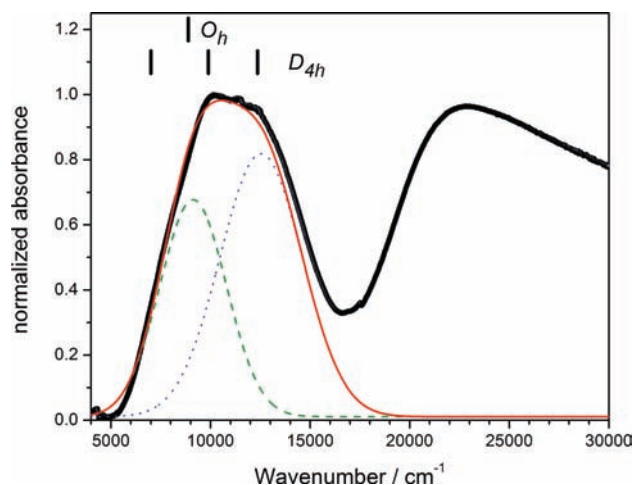

Figure 5. vis−NIR spectrum for $BaAg_2Cu[VO_4]_2$ with the calculated band maxima for O_h and D_{4h} symmetry (lined markers), a Gaussian fit representing the two transitions to $^2B_{2g}(xy)$ (green, dashed line) and $^2E_g(xz, yz)$ (blue, dotted line) with the overall fit (red, solid line) given as well. From a fit to the high-energy part of the spectrum for $BaAg_2Cu$-$[VO_4]_2$ (not included here) a band gap of ≈ 2.3 eV is estimated.

For Ag2 connectivity to the fifth oxygen is established within one segment (intralayer). Both Ag atoms contribute to the interlayer connectivity through O5 and O6, which are not linked to copper.

Physical Properties. The ground state of Cu^{2+} in an axial elongated $4 + 2$ coordination (D_{4h} symmetry) as present in the title compound has been investigated by X-band ESR spectroscopy. Figure 4 shows the measured spectrum with the two components of the g-value, $g_\perp = 2.10$ and $g_{||} = 2.37$, respectively, in agreement with a $^2B_{1g}(x^2-y^2)$ ground state. Considering an average orbital reduction factor of $k = 0.8$ and the spin−orbit coupling parameter for Cu^{2+} of $\zeta = 830$ cm^{-1}, the splitting of the d-orbital set in first order can be estimated.[26] The energy sequence of $d_{xz}, d_{yz} < d_{xy} < d_{z^2} < d_{x^2-y^2}$ gives rise to transitions from $^2B_{1g}(x^2-y^2)$ to $^2B_{2g}(xy)$ and $^2E_g(xz, yz)$ at ≈ 10800 cm^{-1} and ≈ 11550 cm^{-1}, respectively. In fact, these two transitions have been observed in the vis−NIR part of the electromagnetic

spectrum (Figure 5). The shown normalized spectrum includes a Gaussian fit to two d-d transition bands (12538 cm^{-1}, 9125 cm^{-1}) and the overall fit to the asymmetric broad band located at approximately 11300 cm^{-1}.

Furthermore, we have calculated the g-values and the transition energies by applying the AOM[12] using the ligand-field program CAMMAG.[27] We note that for an idealized octahedral complex the (anti-) bonding parameters e_σ and e_π presenting the $\sigma-$ and $\pi-$ interaction, respectively, are related to the ligand field splitting parameter $\Delta = 3e_\sigma - 4e_\pi \approx 8800$ cm^{-1}.[26] On the general basis that these parameters are dependent on the interatomic distance, d, by a d^{-5} relation,[28] we estimated e_σ and e_π to be 6500 cm^{-1}, 2400 cm^{-1} for the equatorial (short) Cu−O distances, and 3000 cm^{-1}, 1250 cm^{-1} for the axial (long) ones, respectively. We calculated the transitions to the excited states $^2E_g(xz, yz)$, $^2B_{2g}(xy)$, and $^2A_{1g}(z^2)$ at 12200 cm^{-1}, 9900 cm^{-1}, and 7000 cm^{-1}, respectively, in accord with the observation. The positions of the calculated bands are included in Figure 5 for idealized O_h and the present D_{4h} symmetry. Including the above-mentioned orbital reduction factor, k, and the spin-orbit coupling parameter, ζ, we derived a splitting of the double degenerate state, $^2E_g(xz, yz)$, of 600 cm^{-1} ("Bethe" notation of the irreducible representations: $\Gamma_6 = 12665$ cm^{-1} and $\Gamma_7 = 12061$ cm^{-1}). This is also reflected by the difference in the bandwidth of the Gaussian fit for the higher energy transition, see Figure 5. The calculated transitions to the $^2A_{1g}(z^2)$ and $^2B_{2g}(xy)$ excited states are almost unchanged for considering first and second order spin-orbit coupling. The derived g-values corresponding to $g_\perp = 2.07$ and $g_{||} = 2.38$ with $g_{av} = 2.18$ are in line with our observed ones, see Figure 4.

In summary, the experimental data and assignments are typical for Cu^{2+} in an axial elongated coordination of oxygen with similar values for $g_\perp \approx 2.10$ and larger ones for $g_{||} \approx 2.45$ reported for $[Cu(H_2O)_6]^{2+}$.[26,29] On the other hand, if we compare with Egyptian Blue, $CaCuSi_4O_{10}$, exhibiting an example for a truly square-planar $[CuO_4]$ complex, striking similarities of the g-values are evident: $g_\perp = 2.07$ and $g_{||} = 2.33$,[30] placing our experimental results for the g-values just in between those limits set by $CaCuSi_4O_{10}$ and $[Cu(H_2O)_6]^{2+}$. For $CaCuSi_4O_{10}$, the void space in the axial direction related to the vanishing antibonding interaction, shifts the transitions to the excited states $^2E_g(xz, yz) = 16130$ cm^{-1} and $^2B_{2g}(xy) = 12740$ cm^{-1} to higher energies. Since the latter transition is connected to $g_{||}$ in first order,[26] and only affected by the equatorial ligand-field parameters, e_σ and e_π, a consistent ligand field splitting can be derived for the $[CuO_4]$ plaquette in these vanadates and silicates for similar Cu−O^{eq} distances of approximately 1.97 Å. On the other hand, the energy of $^2A_{1g}(z^2) = 18520$ cm^{-1} for $CaCuSi_4O_{10}$ is shifted significantly to higher energies when compared to $BaAg_2Cu[VO_4]_2$, leading to the conclusion that in fact the axial ligands need to be taken into account in our case. In particular noteworthy is that the average g-value corresponding to 2.18 for $BaAg_2Cu[VO_4]_2$ is in excellent agreement with the exchange narrowed ESR signal observed for the quasi 1D $S = \frac{1}{2}$ Heisenberg compound $AgCuVO_4$ containing the almost identical structural feature for the $[CuO_{4+2}]$ complex.[5]

On the basis of the overall consistency of our calculations, using the ligand field approach, to describe the isolated complex compared to the experimental data, we have furthermore derived the temperature dependent susceptibility as well. In Figure 6 the measured inverse susceptibility corrected for diamagnetic core contributions ($\chi_o = -1.84 \times 10^{-4}$ emu/mol) versus temperature
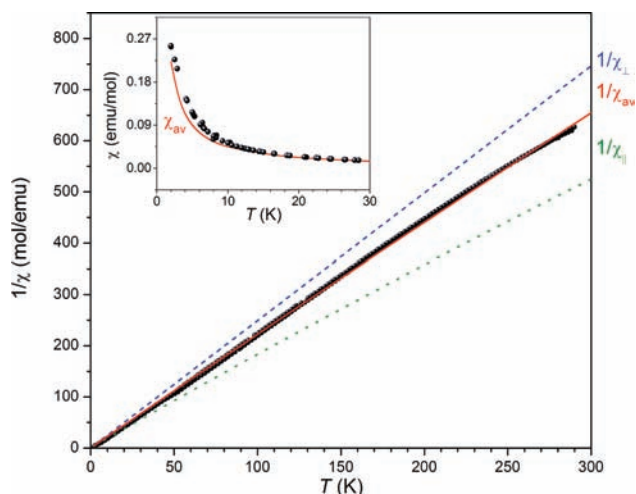
Figure 6. Inverse susceptibility for $BaAg_2Cu[VO_4]_2$ is shown in the main panel with the calculated values for $1/\chi_\perp$ (blue, dashed), $1/\chi_\parallel$ (green, dotted), and $1/\chi_{av}$ (red, solid) for comparison. The inset displays the measured and calculated average susceptibility in the low temperature regime.

Figure 7. Field dependence of the magnetization for $BaAg_2Cu[VO_4]_2$ is shown for temperatures of 2 K (black), 4 K (cyan), 5 K (red), 10 K (blue), and 15 K (green) in comparison with the Brillouin functions (dashed lines, color coded for the respective temperatures).

Figure 8. Top panel: Specific heat divided by the temperature, $C_p/T(T)$, for $BaAg_2M[VO_4]_2$ with M = Cu and Mg. The temperature of the FM long-range order is indicated by T_{LRO}. Left bottom panel: The field dependence of the magnetic part of the specific heat, $C_m(T)$, divided by the gas constant, R, for $BaAg_2Cu[VO_4]_2$ is shown. Indicated are T_{LRO} (3D) and T_{max} (low-dimensional correlations associated with 2D). Right bottom panel: The magnetic entropy derived from integrating C_m/T is depicted for two fields in comparison with the theoretical value for a $S = {}^1/_2$ spin system (dotted lines).

at 1 T (zfc, fc) is plotted together with our calculation of the average and anisotropic components ($\chi_{av}, \chi_\perp, \chi_\parallel$) as a function of the temperature within the angular-overlap model. It can be noted that $BaAg_2Cu[VO_4]_2$ shows an almost ideal paramagnetic behavior at first glance, which is not expected at all based on a $S = {}^1/_2$ AFM Heisenberg chain with SSE constants, J_{intra}, of approximately 100 to 150 K as described for several phosphates[6] exhibiting almost the same bridging feature as observed here for the [100] direction. At $T > 100$ K the experimental inverse susceptibility matches the $1/\chi_{av}$ calculated data with a slope of $C_{av}^{-1} = 0.446^{-1}$ emu^{-1} K^{-1} mol in agreement with the experimental g_{av}-value. A fit to a Curie–Weiss law, $\chi(T) = C/(T - \Theta)$, yields a Curie constant of 0.463(9) emu·K/mol and $\Theta = -5(1)$ K indicative of dominant AFM interactions. Below 50 K a gradual deviation of the experimental $\chi(T)$ from the calculated $\chi_{av}(T)$ occurs and is shown in the inset of Figure 6. The steeper increase in $\chi(T)$ compared to the calculated pure paramagnetic values of χ_{av} can be attributed to the onset of an effective ferromagnetic-like behavior, often observed for competing AFM coupled spins in frustrated systems or onset of ferromagnetic long-range order in principle.

To gain more insight into this problem we have measured the magnetization at several temperatures up to 5 T, which is depicted in Figure 7. For the experimental data at 2 K it can be seen that above 2.5 T the field dependent magnetization change is small up to 5 T, and it is not reaching the saturation value ($M_{sat} \approx 1.09$ μ_B/mol$_{Cu}$ = $Ng\mu_B S$ with $g = 2.18$), typical of an AFM and in accordance with the derived Θ-value above. At lower fields though the magnetization is strongly nonlinear, and a significant enhancement over the $S = {}^1/_2$ Brillouin function is observed. Since $M(H)$ is larger in the field range below ≈ 1.5 T than expected for uncorrelated paramagnetic species, effective ferromagnetic interactions seem to be present. Our measurements of the field dependent magnetization up to 15 K indicate that well above ≈ 10 K the static magnetization almost follows the Brillouin function in the entire measured field range, but with a slightly steeper slope. This leads to the assumption that low-dimensional AFM correlations are largely suppressed at $T \geq 10$ K in fields up to 5 T, and an overall weak FM-like behavior is being
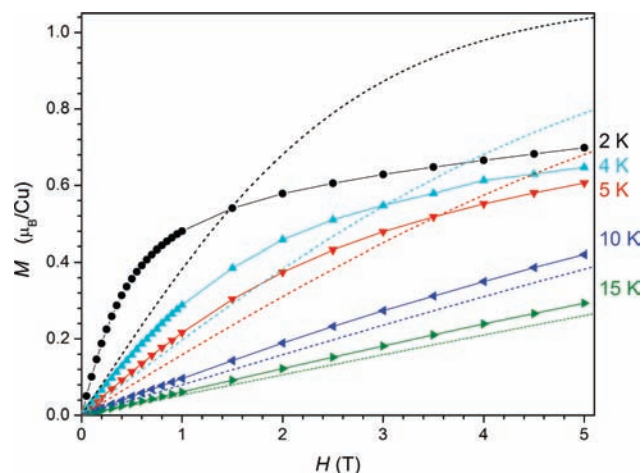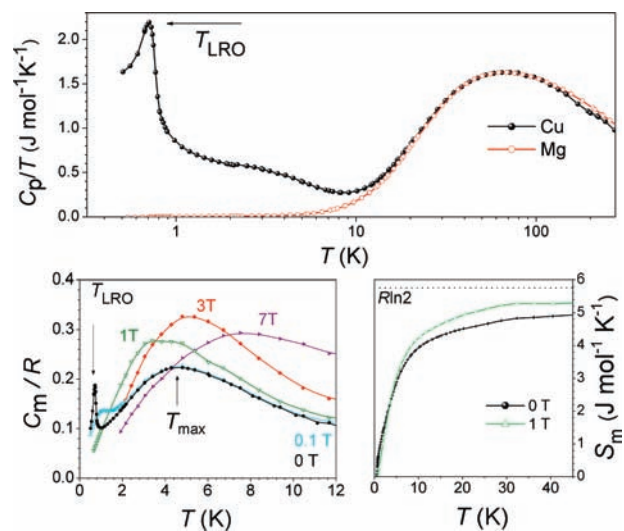
conserved. The question arises whether the FM/AFM spin correlations may result in a magnetically long-range ordered state below the lowest temperature (2 K) of the magnetic measurements. Further insights are obtained by measurements of the specific heat for $BaAg_2Cu[VO_4]_2$ down to 0.5 K (Figure 8) revealing a λ-anomaly at $T_{LRO} \approx 0.72$ K in zero field as the thermodynamic signature of a magnetic phase transition. To estimate the magnetic contribution to the specific heat the lattice part has to be determined reliably. We have therefore synthesized the non-magnetic $BaAg_2Mg[VO_4]_2$ and measured the specific heat of this reference compound (Figure 8, top panel). Using the principle of corresponding states,[31] it is quite safe to correct the

data for the rather small lattice contributions at these low temperatures by subtracting the experimental $C_p(T)$ of non-magnetic $BaAg_2Mg[VO_4]_2$ to extract the principal features for the magnetic part of the specific heat, $C_m(T)$. The bottom left panel of Figure 8 depicts the field dependent $C_m(T)$ data as well and gives evidence of the field induced broadening and vanishing of the λ-anomaly at fields of ≈ 1 T by finally merging with the broad maximum located at approximately $T_{max} \approx 4.5$ K at $\approx 2-3$ T. Further increase of the field shifts the broad feature to higher temperatures. This behavior corroborates a ferromagnetic phase transition at T_{LRO} in zero-field with a release of less than 10% of the total spin entropy expected for a $S = {}^1/_2$ system. At $T_{max} \approx 4.5$ K an almost symmetric broad maximum is present at all fields, and it is interesting to note that in zero-field (a) at C_m^{max} approximately half of the entire spin-entropy for a $S = {}^1/_2$ system is released, and (b) the value of $(C_m/R)^{max} \approx 0.22$ is in excellent agreement with 0.22 expected from theory for the AFM $S = {}^1/_2$ triangular lattice.[32] Thus, our experiments strongly suggest that $BaAg_2Cu[VO_4]_2$ does not belong to the class of quasi-1D systems for which theory predicts a significant larger value of 0.35 for $(C_m/R)^{max}$ in zero-field.[33]

The bottom right panel of Figure 8 shows the derived spin entropy $S_m(T)$, from the integration of $C_m(T)/T$ at $H = 0$ T and 1 T in accordance with the expected value of $S_m = R \ln 2$ as the high temperature limit. Furthermore, it is evident that the entropy associated with the λ-anomaly at T_{LRO} is shifted to higher temperatures with increasing fields. Overall, the presence of short-range (2D) AFM correlations and long-range three-dimensional (3D) magnetic order are evident.

On the basis of these observations, one might speculate if strong quantum fluctuations could be effective, prevailing long-range order at higher temperatures and placing this compound into the category of a promising candidate within the class of low-dimensional (geometrically) frustrated spin systems.

4. CONCLUSIONS

We have synthesized $BaAg_2Cu[VO_4]_2$ presenting a new structure type within the $BaA_2M[VO_4]_2$ family of compounds with A = Na, Ag; M = Mn, Cu. Flux growth methods have been employed to grow single crystals including a low-temperature oxidation of silver metal. Structure-property relationships are reported and ligand-field calculations (AOM) are based on the structure determination from single crystal X-ray data. Infrared data for the ortho-vanadate ions indicate substantial dependence of the connectivity of Cu via O^{eq} within the defined layers in contrast to the pronounced ionic interaction via O5, O6 linked to the non-magnetic counterions, barium and silver. The electronic structure of Cu^{2+} present in $BaAg_2Cu[VO_4]_2$ has been determined from UV-vis-NIR and ESR spectroscopy data, confirming the $^2B_{1g}(x^2-y^2)$ ground state and the excited states in good agreement with the g-values observed and calculated within the AOM. The results of the magnetic measurements indicate weak interactions between the magnetic centers exclusively through asymmetric SSE pathways. The magnetization of $BaAg_2Cu[VO_4]_2$ reveals profound interplay of long-range FM with dominating AFM short-range correlations as indicated by specific heat measurements as well. On the basis of structural considerations and the Cu^{2+} ground state one would expect a 1D AFM chain along [100] (Figure 1 and 2), since the axial d_{z^2} orbital is in most cases considered to be negligible for magnetic interaction. To our surprise the 1D scenario is not supported by

the thermodynamic measurements for $BaAg_2Cu[VO_4]_2$, and we propose that interchain exchange pathways within the layers need to be considered to account for the observed properties in close resemblance to theoretical models for a $S = {}^1/_2$ AFM triangular lattice. Nevertheless, the proposed scenario of low-dimensional competing intra- and interchain exchange interactions (compare with the color codes red and orange, respectively, in the synopsis figure) deserves a more detailed investigation of J_{intra} and J_{inter} in the vicinity of a frustrated spin-system, calling for further local methods (NMR and high-field ESR) and a microscopic description supported from theory.

■ ASSOCIATED CONTENT

ⓢ **Supporting Information.** Table S1 includes final coordinates and equivalent isotropic displacement parameters for $BaAg_2Cu[VO_4]_2$. Table S2 includes selected angles for $BaAg_2Cu[VO_4]_2$. Figure S3 shows an alternating honeycomb arrangement of Ag and V with Cu atoms located below the layer present in $BaAg_2Cu[VO_4]_2$. Figure S4 shows the infrared spectrum of $BaAg_2Cu[VO_4]_2$. Figure S5 shows the field dependence of the magnetic part of the specific heat, $C_m(T)$, divided by the gas constant, R, for $BaAg_2Cu[VO_4]_2$ at fields up to 7 T. This material is available free of charge via the Internet at http://pubs. acs.org. X-ray crystallographic files in CIF format for the structure determination of $BaAg_2Cu[VO_4]_2$ are available from the Fachinformationszentrum Karlsruhe, 76344 Eggenstein-Leopoldshafen, Germany (e-mail: crysdata@fiz-karlsruhe.de, http://www.fiz-karlsruhe.de/request_for_deposited_data.html) by quoting the deposition number, CSD-422132.

■ AUTHOR INFORMATION

Corresponding Author
*E-mail: amoeller@uh.edu.

■ ACKNOWLEDGMENT

■ REFERENCES

(1) Dagotto, E.; Rice, T. M. *Science* **1996**, *271*, 618–623.
(2) Goodenough, J. B. In *Magnetism and the Chemical Bond*; Wiley: Cambridge, MA, 1963.
(3) (a) Koo, H.-J.; Dai, D.; Whangbo, M.-H. *Inorg. Chem.* **2005**, *44*, 4359–4365. (b) Koo, H.-J.; Whangbo, M.-H. *Inorg. Chem.* **2006**, *45*, 4440–4447.
(4) Rosner, H.; Johannes, M. D.; Drechsler, S.-L.; Schmitt, M.; Janson, O.; Schnelle, W.; Liu, W.; Huang, Y.-X.; Kniep, R. *Sci. Technol. Adv. Mater.* **2007**, *8*, 352–356.
(5) Möller, A.; Schmitt, M.; Schnelle, W.; Förster, T.; Rosner, H. *Phys. Rev. B* **2009**, *80*, 125106-8.
(6) Nath, R.; Mahajan, A. V.; Büzzgen, N.; Kegeler, C.; Loidl, A. *Phys. Rev. B* **2005**, *71*, 174436-11.
(7) Belik, A. A.; Azuma, M.; Matsuo, A.; Kindo, K.; Takano, M. *Inorg. Chem.* **2005**, *44*, 3762–3766.
(8) (a) Rettich, R.; Müller-Buschbaum, Hk. *Z. Naturforsch.* **1998**, *53b*, 291–295. (b) Müller-Buschbaum, Hk. *Z. Anorg. Allg. Chem.* **2004**, *630*, 2125–2175.

2213

dx.doi.org/10.1021/ic1018554 |*Inorg. Chem.* 2011, 50, 2207–2214

(9) von Postel, M.; Müller-Buschbaum, Hk. *Z. Anorg. Allg. Chem.* **1992**, *618*, 107–110.

(10) Nath, R.; Tsirlin, A. A.; Rosner, H.; Geibel, C. *Phys. Rev. B* **2008**, *78*, 064422–7.

(11) Drechsler, S.-L.; Volkova, O.; Vasiliev, A. N.; Tristan, N.; Richter, J.; Schmitt, M.; Rosner, H.; Málek, J.; Klingeler, R.; Zvyagin, A. A.; Büchner, B. *Phys. Rev. Lett.* **2007**, *98*, 077202-4.

(12) (a) Schäffer, C. E.; Jørgensen, C. K. *Mol. Phys.* **1965**, *9*, 401–412. (b) Richardson, D. E. *J. Chem. Educ.* **1993**, *70*, 372–380.

(13) Vogt, R.; Müller-Buschbaum, Hk. *Z. Anorg. Allg. Chem.* **1990**, *591*, 167–173.

(14) Rodriguez-Cavajal, J. *FullProf2000*, Vers. 4.80; Laboratoire Léon Brillouin CEA-CNRS: Gif-sur-Yvette Cedex, France, 2009; http://www.ill.eu/sites/fullprof/.

(15) Blessing, R. H. *Acta Crystallogr.* **1995**, *A51*, 33–38.

(16) Farrugia, L. J.*WinGX, An Integrated System of Windows Programs for Solution, Refinement and Analysis of Single Crystal X-ray Diffraction Data*, Vers. 1.80.05; *J. Appl. Crystallogr.* 1999, 32, 837−838.

(17) (a) Sheldrick, G. M. *SHELXS-97, SHELXL-97*; University of Göttingen: Göttingen, Germany, 1997.(b) Sheldrick, G. M. *Acta Crystallogr.* **2008**, *A64*, 112–122.

(18) (a) Spek, A. L. *J. Appl. Crystallogr.* **2003**, *36*, 7–13. (b) Spek, A. L. *Acta Crystallogr.* **2009**, *D65*, 148–155.

(19) Brandenburg, K. *Diamond - Crystal and Molecular Structure Visualization*, Vers. 3.2e; Crystal Impact GbR: Bonn, Germany, 1997−2010.

(20) (a) Hoppe, R. In *Crystal Structure and Chemical Bonding in Inorganic Chemistry*; Rooymans, C. J. M.; Rabenau, A., Ed.; North-Holland: Amsterdam, The Netherlands, 1975; pp 127−161.(b) Hoppe, R. *Angew. Chem., Int. Ed. Engl.* **1970**, *9*, 25–34.(c) Hübenthal, R. *MAPLE*, Vers. 4; Universität Giessen: Giessen, Germany, 1993.

(21) Hoppe, R. *Z. Kristallogr.* **1979**, *150*, 23–52.

(22) Nakamoto, K. In *Infrared and Raman Spectra of Inorganic and Coordination Compounds*, 3rd ed; Wiley-Interscience, John Wiley & Sons, Inc.: New York, 1978.

(23) Hardcastle, F. D.; Wachs, I. E. *J. Phys. Chem.* **1991**, *95*, 5031–5041.

(24) Kerp, O.; Möller, A. *Z. Anorg. Allg. Chem.* **2006**, *632*, 1187–1194.

(25) Shannon, R. D. *Acta Crystallogr.* **1976**, *A32*, 751–767.

(26) Figgis, B. N.; Hitchman, M. A. In *Ligand Field Theory and its Applications*; Wiley-VCH: New York, 2000.

(27) (a) Gerloch, M. *Magnetism and Ligand Field Theory*; Cambridge University Press: Cambridge, U.K., 1983.(b) Gerloch, M.; McMeeking, R. F. *J. Chem. Soc., Dalton Trans.* 1975, 2443–2451.(c) Kruse, D. A.; Davis, J. E.; Gerloch, M.; Harding, J. H.; Mackey, D. J.; McMeeking, R. F. *CAMMAG*, FORTRAN computing package; University Chemical Laboratory: Cambridge, England, 1979.

(28) Bermejo, M.; Pueyo, L. *J. Chem. Phys.* **1983**, *78*, 854–857.

(29) Bencini, A.; Gatteschi, D. In *Inorganic Electronic Structure and Spectroscopy*; Solomon, E. I., Lever, A. B. P., Eds.; John Wiley& Sons, Inc.: New York, 1999; Vol. 1, Chapter 2.

(30) Ford, R. J.; Hitchman, M. A. *Inorg. Chim. Acta* **1979**, *33*, L167–L170.

(31) Stout, J. W.; Catalano, E. *J. Chem. Phys.* **1955**, *23*, 2013–2022.

(32) Bernu, B.; Misguich, G. *Phys. Rev. B* **2001**, *63*, 134409–9.

(33) Klümper, A.; Johnston, D. C. *Phys. Rev. Lett.* **2000**, *84*, 4701–4704.